

SAC-Net: Spatial Attenuation Context for Salient Object Detection

Xiaowei Hu, Chi-Wing Fu, *Member, IEEE*, Lei Zhu, and Pheng-Ann Heng, *Senior Member, IEEE*

Abstract—This paper presents a new deep neural network design for salient object detection by maximizing the integration of local and global image context within, around, and beyond the salient objects. Our key idea is to adaptively propagate and aggregate the image context features with variable attenuation over the entire feature maps. To achieve this, we design the spatial attenuation context (SAC) module to recurrently translate and aggregate the context features independently with different attenuation factors and then to attentively learn the weights to adaptively integrate the aggregated context features. By further embedding the module to process individual layers in a deep network, namely SAC-Net, we can train the network end-to-end and optimize the context features for detecting salient objects. Compared with 29 state-of-the-art methods, experimental results show that our method performs favorably over all the others on six common benchmark data, both quantitatively and visually.

Index Terms—Spatial attenuation context, salient object detection, saliency detection, deep learning.

I. INTRODUCTION

Salient object detection is an effective and useful pre-processing step in many image processing and computer vision tasks, *e.g.*, object segmentation [1] and tracking [2], video compression [3] and abstraction [4], image editing [5], texture smoothing [6], as well as few-shot learning [7]. It is a fundamental problem in computer vision research and has been extensively studied in the past decade.

Early works attempt to detect salient objects based on low-level cues like contrast, color, and texture [8], [9], [10]. However, relying on low-level cues is clearly inadequate to finding salient objects, which involve high-level semantics. Hence, most recent methods [11], [12], [13], [14], [15] employ convolutional neural networks (CNNs) and take a data-driven approach to the problem by leveraging both high-level semantics and low-level details extracted from multiple CNN layers [16], [17], [18], [19], [20], [21], [22], [23], [24], [25], [26], [27], [28], [29], [30], [31]. However, since the convolution operator in CNN processes a local neighborhood in the spatial domain [32], existing methods tend to miss global spatial semantics in the results, *e.g.*, they may misrecognize background noise as salient objects; see Section IV-B for quantitative and qualitative comparisons.

Essentially, salient objects are key elements that stand out from the background. Such an inference process [33] should

X. Hu and L. Zhu are with the Department of Computer Science and Engineering, The Chinese University of Hong Kong.

C.-W. Fu and P.-A. Heng are with the Department of Computer Science and Engineering, The Chinese University of Hong Kong and Guangdong Provincial Key Laboratory of Computer Vision and Virtual Reality Technology, Shenzhen Institutes of Advanced Technology, Chinese Academy of Sciences, China.

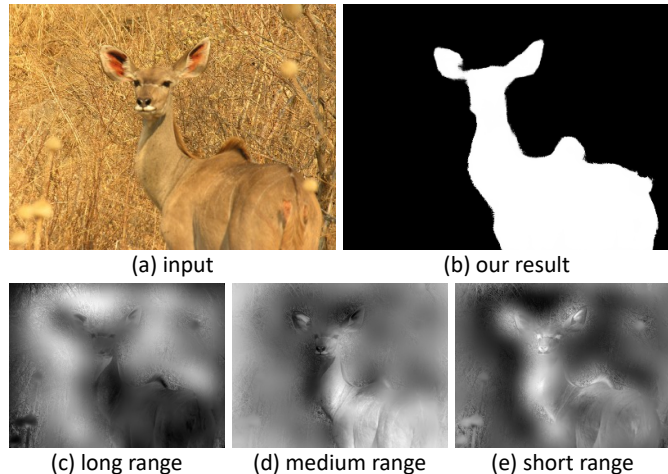


Fig. 1: A challenging example (a), where our method is still able to find the object contour (b); see (c)-(e) for the attention weights learned for different spatial ranges.

involve not only the local image context within and around the salient objects, but also the global image context, as well as a suitable integration of the various context features. Ideally, after extracting context features per image pixel, if we can connect all these features and let them communicate with every other over the spatial domain, we can optimize the feature integration for maximized performance. However, it is computationally infeasible in practice. Hence, we propose to propagate context features with different attenuation factors over the image and learn to aggregate the resulting features adaptively; by then, our network can learn to detect salient objects by adaptively considering context features within, around, and even far from, the salient objects.

Figure 1 shows a challenging example with the associated attention maps learned in our network for *integrating the various image context*: long-range context aggregated with a small attenuation factor (c) to help locate the global background; medium-range context (d) to help identify the image regions of the same object; and short-range context aggregated with a large attenuation factor (e) to help locate the boundary between salient and non-salient regions.

To this end, we formulate the *spatial attenuation context module*, or *SAC module* for short, in a deep network to allow the image features in a CNN to *propagate over variable spatial ranges by articulating different attenuation factors in the propagation*. Our module has two rounds of recurrent translations to propagate and aggregate the image features.

In each round, we propagate features independently using different attenuation factors towards different directions in the spatial domain; further, we formulate an attention mechanism to learn the weights to combine the aggregated features. Hence, we can adopt different attenuation factors (or influence ranges) for different image features. Furthermore, we deploy a SAC module in each layer of our network and predict a saliency map per layer based on the output from the SAC module and the convolutional features. Below, we summarize the major contributions of this work:

- First, we design the spatial attenuation context (SAC) module to recurrently propagate the image features over the whole feature maps with variable attenuation factors and learn to adaptively integrate the features through an attention mechanism in the module.
- Second, we adopt the SAC module in each layer of our network architecture to learn the spatial attenuation context in different layers, and train the whole network in an end-to-end manner for salient object detection.
- Lastly, we evaluate our method and compare it against 29 state-of-the-art methods on six common benchmark data. Results show that our method performs favorably over all the others for all the benchmark data. *We will release our code, the trained models, and the predicted saliency maps on all the benchmark datasets upon the publication of this work.*

II. RELATED WORK

Rather than being comprehensive, we discuss mainly the methods on single-image salient object detection. Early methods use hand-crafted priors such as image contrast [9], [34], color [35], [36], texture [37], [38], and other low-level visual cues [39]; see [40] for a survey. Clearly, hand-crafted features are insufficient to capture high-level semantics, so methods based on them often fail for nontrivial inputs.

Recent works [11], [12], [13], [14], [15] exploit convolutional neural networks (CNN) to learn deep features for detecting salient objects. Zhao *et al.* [15] used a fully-connected CNN to find and combine global and local features to predict saliency maps. Wang *et al.* [13] developed a recurrent CNN with the prediction map from the previous recurrent step as the guidance. Zhang *et al.* [14] adopted a dropout technique to learn deep uncertain convolutional features in the network to enhance its generalization capability. However, since these methods just take features at deep CNN layers, they tend to miss the details in the salient objects, which are captured mainly in the shallow layers.

Several recent works [20], [18], [23], [19], [17], [22], [24], [21], [16], [41], [25] enhance the detection quality by further integrating features in multiple CNN layers to simultaneously leverage more global and local context in the inference process. Among them, Li *et al.* [20] explored the semantic properties and visual contrast of salient objects, Hou *et al.* [18] created short connections to integrate features in different layers, while Zhang *et al.* [23] derived a resolution-based feature combination module and a boundary-preserving refinement strategy. Hu *et al.* [19] recurrently aggregated deep

features to exploit the complementary saliency information between the multi-level features and the features at each individual layer. Later, Deng *et al.* [17] adopted residual learning to alternatively refine features at deep and shallow layers. Zhang *et al.* [22] formulated a bi-directional message passing model to select features for integration. Zhang *et al.* [24] designed an attention-guided network to progressively select and integrate multi-level information. Li *et al.* [21] used a two-branch network to simultaneously predict the contours and saliency maps. Chen *et al.* [16] leveraged residual learning and reverse attention to refine the saliency maps. Zhang *et al.* [25] designed a symmetrical CNN to learn the complementary saliency information and presented a weighted structural loss to enhance the boundaries of salient objects. Wang *et al.* [41] explored the global and local spatial relations in deep networks to locate salient objects and refine the object boundary. Although the detection quality keeps improving, the exploration of global spatial context, particularly in the shallow layers, is still heavily limited by the convolution operator in CNN, which is essentially a local spatial filter [32].

Very recently, Liu and Han [42] incorporated global context and scene context by developing a deep spatial long short-term memory model. Liu *et al.* [43] aggregated the attended contextual features from a global/local view in feature maps of varying resolutions. Wang *et al.* [26] presented a pyramid attention structure and leveraged the salient edge information to better segment salient objects. Feng *et al.* [44] designed an attentive feedback network to further explore the boundaries of the salient objects. Zhao and Wu [27] used the dilated convolution and channel-wise & spatial attention to aggregate multi-scale context features. Wu *et al.* [28] proposed to discard the feature maps at shallow layers for acceleration and used the saliency map generated from one network branch to refine the features of another branch. Liu *et al.* [29] introduced two pooling-based modules to progressively refine the highly semantic features for detail enriched saliency maps. Wang *et al.* [30] predicted the saliency maps by iteratively aggregating the feature maps in the top-down and bottom-up manner. Zhang *et al.* [45] incorporated the semantic information of salient objects from the image captions. Qin *et al.* [46] formulated a boundary-aware salient object detection network by combining a deeply supervised encoder-decoder and a residual refinement module, and leveraged a hybrid loss to optimize the whole network. Wu *et al.* [31] jointly performed foreground contour detection and edge detection tasks by using multi-task intertwined supervision. Even the detection performance continues to improve on the benchmarks [47], [48], [49], [50], [37], [38], current methods may still miss local parts in salient objects and misrecognize noises in non-salient regions as salient objects.

Beyond the recent works [41], [42], [43] that emphasize the importance of reasoning spatial context for salient object detection, we leverage and selectively aggregate surrounding image context spatially in the same CNN layer by a new concept, i.e., attentively allowing the context features to recurrently translate with varying attenuation factors.

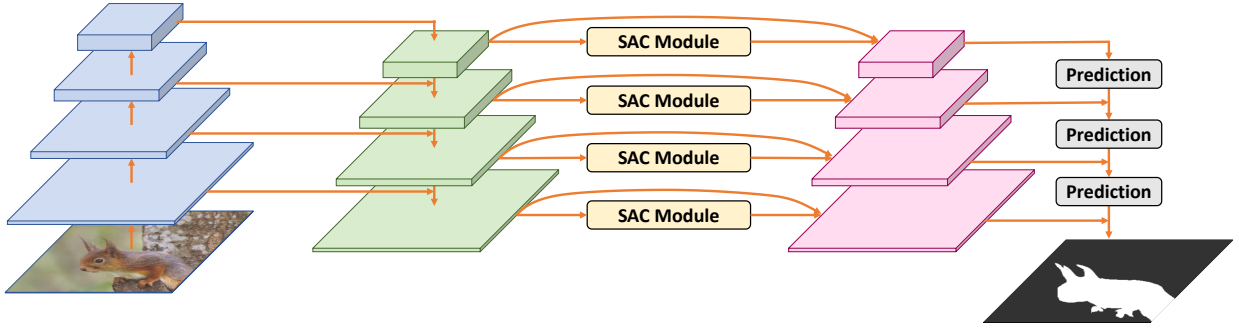


Fig. 2: The schematic illustration of our spatial attenuation context network (SAC-Net): (i) extract feature maps (in blue) in different resolutions from the input image using a convolutional neural network; (ii) construct a feature pyramid (in green) by successively upsampling the feature map at a deep layer and combining the upsampled result with the feature map at an adjacent shallower layer; (iii) use SAC modules (see Figure 4) to generate spatial attenuation context features for each layer; (iv) concatenate the outputs from the SAC modules with the convolutional features (in red); and (v) lastly, successively predict a saliency map at each layer and take the final saliency map of the largest resolution as the network output. In the figure, feature maps are indicated by blocks and thicker blocks of smaller sizes are higher-level features at deeper layers.

III. METHODOLOGY

Figure 2 outlines the architecture of our spatial attenuation context network (SAC-Net), which takes a whole image as input and predicts the saliency map in an end-to-end manner. First, we use a CNN to generate feature maps in different resolutions and progressively propagate the image features at deep layers to feature maps at shallow layers to construct a feature pyramid [51]. After that, we use our SAC modules to harvest spatial attenuation context per layer and concatenate the module outputs with the corresponding convolutional features. Lastly, we predict a result per layer, upsample and merge it with the shallower-layer output, and take the result of the largest resolution as the final network output. In the following subsections, we first elaborate on the SAC module, and then present the strategies to train and test our network for salient object detection.

A. Spatial Attenuation Context Module

Figure 4 shows the architecture of the *spatial attenuation context module*, or *SAC module*, which takes a feature map as input and produces spatial attenuation context in the same resolution. As presented earlier, the spatial attenuation context contains image context aggregated by propagating local image context using varying attenuation factors via an attention mechanism; hence, we can disperse the local image context adaptively over the whole feature maps.

See again the SAC module in Figure 4. First, we use a 1×1 convolution on the input feature map to reduce the number of feature channels. Then, we adopt recurrent translations with varying attenuation factors (α_k) to disperse the local image features in four different directions; see the illustration in Figure 3(b) & the detailed structure of recurrent translations in Figure 4. At this moment, each pixel learns the spatial attenuation context along the four directions. After two rounds of recurrent translations, we adaptively disperse the local features over the 2D domain; see Figure 3(c). Hence, each pixel knows *the global spatial attenuation context over the*

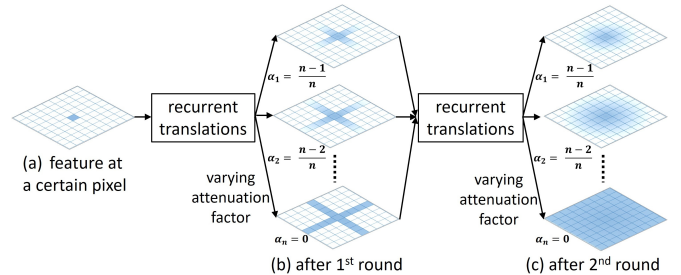


Fig. 3: Illustrating how the image features propagate with varying attenuation factors (α_k) inside the SAC module; please see Figure 4 for the detailed module architecture.

entire feature map. More importantly, we learn the weights to combine the recurrently-aggregated results via an attention mechanism in an end-to-end manner (Figure 4), so each pixel in the SAC module output can receive spatial context *adaptively* from its surroundings.

Recurrently-attenuating translation. To optimize the dispersal of local context, we first formulate a parametric model to recurrently aggregate the image features with attenuation. Given the feature map after a 1×1 convolution (see Figure 4), we recurrently translate its features using different attenuation factors α_k in four principal directions: left, up, right, and down. Moreover, to ensure manageable memory consumption, we set the number of feature channels in each recurrently-aggregated feature map as $\lfloor \frac{256}{n} \rfloor$, where n is the number of different attenuation factors in the SAC module; see Table IV for an experiment on n .

Denoting $f_{i,j}$ as the feature at pixel (i, j) in a feature map, our recurrently-attenuating translation process propagates features progressively over the spatial domain using the following equation (typically in the up direction) :

$$\begin{aligned} f_{i,j}^{up}(\alpha_k, \beta) &= \max(r_{i,j}^{up}, 0) + \beta \min(r_{i,j}^{up}, 0) \\ \text{and } r_{i,j}^{up} &= (1 - \alpha_k) \cdot f_{i-1,j}^{up} + f_{i,j}, \end{aligned} \quad (1)$$

where $\alpha_k = \frac{n-k}{n}$ ($k \in \{1, 2, \dots, n\}$) is the attenuation factor,

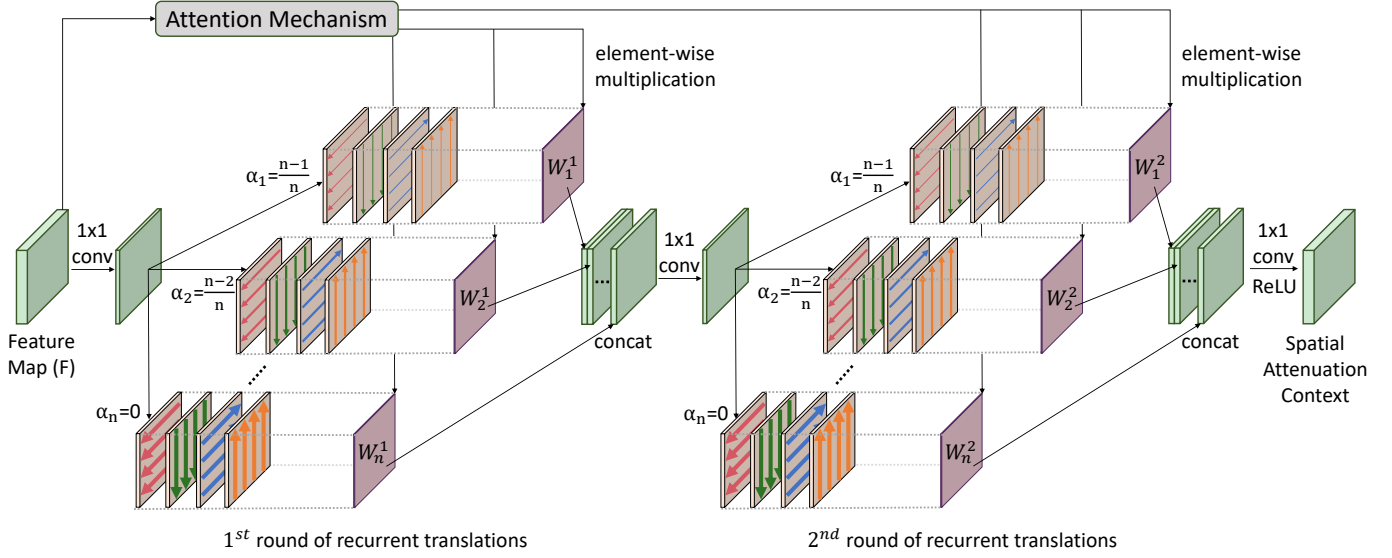


Fig. 4: The schematic illustration of the spatial attention context (SAC) module. We adopt two rounds of recurrent translations to propagate and aggregate image features. In each round, the colored arrows show the recurrent translation direction, while thicker (or thinner) arrows indicate stronger (or weaker) information propagation with less (or more) attenuation.

and β is a learnable parameter in our recurrently-attenuating translation model.

In Eq. (1), we recurrently aggregate image features by using $r_{i,j}^{up}$, where a smaller α_k (close to zero) allows the features to propagate over a longer distance, while a larger α_k (close to one) limits the propagation, so the related local features affect a smaller local area; see again the illustration in Figure 3. Moreover, when $r_{i,j}^{up} < 0$, the first term in $f_{i,j}^{up}$ will become zero, and β will be multiplied with $r_{i,j}^{up}$. We define β in Eq. (1) to reduce the feature magnitude when it is negative. Since we learn the value of β for each feature channel, we can introduce nonlinearities when aggregating the spatial context and express more complex relations among the local features. Note that in our experiments, we initialize β as 0.1 for all the feature channels and learn it automatically during the network training process; in practice, we found that β rarely goes beyond one in our experiments.

Attention mechanism. After recurrently-translating the input feature map using different attenuation factors in four directions, we will obtain $4n$ feature maps; see the feature maps with colored arrows in Figure 4. As discussed earlier, the long-range image context reveals global semantics, while the short-range context helps identify the boundary between salient and non-salient regions. To adaptively leverage the complementary advantages of these aggregated spatial context features, we formulate an attention mechanism to learn the weights for selectively integrating them.

As shown at the top left corner in Figure 4, we take the input feature map F as the input to the attention mechanism and produce a set of unnormalized attention weights $\{A_1^1, A_2^1, \dots, A_n^1\}$, each corresponding to a particular attenuation factor; superscript 1 indicates that these weights are for the first round of recurrent translations. Then, we apply the Softmax function (Eq. (3)) to normalize the weights and produce the attention weight maps $\{W_1^1, W_2^1, \dots, W_n^1\}$

associated with different attenuation factors (see Figure 4):

$$\{A_1^1, A_2^1, \dots, A_n^1\} = \mathcal{F}_{attention}(F; \theta), \text{ and} \quad (2)$$

$$w_{i,j,k}^1 = \frac{\exp(a_{i,j,k}^1)}{\sum_k \exp(a_{i,j,k}^1)}, \quad (3)$$

where $a_{i,j,k}^1 \in A_k^1$ is the unnormalized attention weight at pixel (i, j) for attenuation factor α_k , $w_{i,j,k}^1 \in W_k^1$ are the normalized attention weights, and θ denotes the parameters learned by $\mathcal{F}_{attention}$, which consists of two 3×3 convolution layers and one 1×1 convolution layer, and we apply the group normalization [52] and ReLU non-linear operation [53] after the first two convolution layers.

Next, we multiply W_k^1 with the corresponding context features aggregated after the recurrent translations:

$$f_{i,j} = \oplus_{k=1}^n \left[\left(f_{i,j}^{up}(\alpha_k, \beta) \oplus f_{i,j}^{down}(\alpha_k, \beta) \oplus f_{i,j}^{left}(\alpha_k, \beta) \oplus f_{i,j}^{right}(\alpha_k, \beta) \right) \times w_{i,j,k}^1 \right], \quad (4)$$

where \times denotes an element-wise multiplication, \oplus denotes the concatenation operator, and $\oplus_{k=1}^n$ concatenates all the feature maps for different attenuation factors, after the feature maps are multiplied with the attention weights ($w_{i,j,k}^1$). With the attention weights learned to select and integrate the context features aggregated with different attenuation factors (see again Figure 1), our network can adaptively control the feature integration and allow the context features to be implicitly dispersed over varying spatial ranges.

Completing the SAC module. After concatenating the features, we complete the first round of recurrent translations in our SAC module and further apply a 1×1 convolution to reduce the feature channels. Then, we repeat the same process in the second round of recurrent translation using another set of attention weights $\{W_1^2, W_2^2, \dots, W_n^2\}$, which are also learnt through the attention mechanism; see again Figure 4. After

TABLE I: Comparing our method (SAC-Net) with 29 state-of-the-art methods using the F_β , S_m and MAE metrics. Top two results are highlighted in **red** and **blue**, respectively; “-” indicates results that are not publicly available on the corresponding dataset; and “*” indicates CRF is used as a post-processing step in the methods.

Dataset & Size	-	ECSSD [37] 1, 000 images			PASCAL-S [48] 850 images			SOD [54] 300 images			HKU-IS [47] 4, 447 images			DUT-OMRON [38] 5, 168 images			DUTS-test [50] 5, 019 images		
		Year	F_β	S_m	MAE	F_β	S_m	MAE	F_β	S_m	MAE	F_β	S_m	MAE	F_β	S_m	MAE	F_β	S_m
SAC-Net* (ours)	-	0.954	0.930	0.028	0.876	0.801	0.070	0.884	0.801	0.092	0.945	0.925	0.023	0.832	0.846	0.050	0.898	0.878	0.032
PiCA-RC* [43]	2018	0.940	0.916	0.035	0.870	0.789	0.073	0.867	0.780	0.094	0.929	0.905	0.031	0.828	0.826	0.054	0.871	0.849	0.040
R ³ Net* [17]	2018	0.935	0.910	0.040	0.845	0.749	0.100	0.847	0.761	0.124	0.916	0.900	0.036	0.805	0.817	0.063	0.833	0.823	0.058
GNLB* [6]	2018	0.931	0.900	0.045	0.840	0.758	0.096	0.837	0.744	0.127	0.917	0.886	0.037	0.800	0.817	0.058	0.830	0.811	0.058
RADF* [19]	2018	0.924	0.894	0.049	0.832	0.754	0.102	0.835	0.759	0.125	0.914	0.889	0.039	0.789	0.815	0.060	0.819	0.814	0.061
DSS* [18]	2017	0.916	0.882	0.053	0.829	0.739	0.102	0.842	0.746	0.118	0.911	0.881	0.040	0.771	0.790	0.066	0.825	0.812	0.057
DCL* [20]	2016	0.898	0.868	0.071	0.822	0.783	0.108	0.832	0.745	0.126	0.904	0.861	0.049	0.757	0.771	0.080	0.782	0.795	0.088
SAC-Net (ours)	-	0.951	0.931	0.031	0.879	0.806	0.070	0.882	0.809	0.093	0.942	0.925	0.026	0.830	0.849	0.052	0.895	0.883	0.034
PoolNet-R [29]	2019	0.944	0.921	0.039	0.865	0.794	0.080	0.869	0.801	0.100	0.934	0.912	0.033	0.830	0.836	0.056	0.886	0.871	0.040
BASNet [46]	2019	0.942	0.916	0.037	0.858	0.785	0.084	0.851	0.772	0.112	0.929	0.909	0.032	0.811	0.836	0.056	0.860	0.853	0.047
CPD-R [28]	2019	0.939	0.918	0.037	0.861	0.789	0.078	0.859	0.771	0.110	0.925	0.906	0.034	0.797	0.825	0.056	0.865	0.858	0.043
AFNet [44]	2019	0.935	0.917	0.042	0.866	0.792	0.076	-	-	-	0.925	0.905	0.036	0.820	0.826	0.057	0.867	0.855	0.045
MLMSNet [31]	2019	0.930	0.909	0.045	0.858	0.790	0.079	0.862	0.790	0.106	0.922	0.906	0.039	0.793	0.809	0.064	0.854	0.851	0.048
CapSal [45]	2019	-	-	-	0.868	0.769	0.079	-	-	-	0.889	0.849	0.057	-	-	-	0.845	0.808	0.060
PiCA-R [43]	2018	0.935	0.917	0.047	0.868	0.800	0.078	0.864	0.793	0.103	0.919	0.904	0.043	0.820	0.832	0.065	0.863	0.859	0.050
ASNet [55]	2018	0.932	0.915	0.047	0.869	0.794	0.075	0.859	0.800	0.105	0.922	0.906	0.041	-	-	-	0.835	0.834	0.060
R ³ Net [17]	2018	0.929	0.910	0.051	0.842	0.761	0.103	0.839	0.770	0.131	0.914	0.897	0.046	0.802	0.819	0.073	0.831	0.829	0.067
BDMPM [22]	2018	0.928	-	0.044	0.862	-	0.074	0.851	-	0.106	0.920	-	0.038	-	-	-	0.850	-	0.049
PAGRN [24]	2018	0.927	0.889	0.061	0.849	0.749	0.094	-	-	-	0.918	0.887	0.048	0.771	0.775	0.071	0.854	0.825	0.055
GNLB [6]	2018	0.926	0.904	0.056	0.841	0.772	0.099	0.834	0.762	0.133	0.909	0.891	0.048	0.800	0.824	0.067	0.821	0.822	0.068
DGRL [41]	2018	0.925	0.906	0.045	0.850	0.796	0.080	0.846	0.777	0.104	0.914	0.897	0.037	0.779	0.810	0.063	0.834	0.836	0.051
RAS [16]	2018	0.916	0.893	0.058	0.842	0.735	0.122	0.847	0.767	0.123	0.913	0.887	0.045	0.785	0.814	0.063	0.831	0.828	0.059
C2S [21]	2018	0.911	0.896	0.053	0.845	0.793	0.084	0.821	0.763	0.122	0.898	0.889	0.046	0.759	0.799	0.072	0.811	0.822	0.062
SRM [56]	2017	0.917	0.895	0.054	0.847	0.782	0.085	0.839	0.746	0.126	0.906	0.888	0.046	0.769	0.798	0.069	0.827	0.825	0.059
Amulet [23]	2017	0.913	0.894	0.059	0.828	0.794	0.095	0.801	0.755	0.146	0.887	0.886	0.053	0.737	0.781	0.083	0.778	0.796	0.085
UCF [14]	2017	0.910	0.883	0.078	0.821	0.792	0.120	0.800	0.763	0.164	0.886	0.875	0.073	0.735	0.758	0.131	0.771	0.777	0.117
NLDF [12]	2017	0.905	0.875	0.063	0.831	0.756	0.099	0.810	0.759	0.143	0.902	0.879	0.048	0.753	0.770	0.080	0.812	0.815	0.066
DHSNet [57]	2016	0.907	0.884	0.059	0.827	0.752	0.096	0.823	0.752	0.127	0.892	0.870	0.052	-	-	-	0.807	0.811	0.067
RFCN [13]	2016	0.898	0.860	0.097	0.827	0.793	0.118	0.805	0.717	0.161	0.895	0.859	0.079	0.747	0.774	0.095	0.784	0.791	0.091
ELD [58]	2016	0.867	0.841	0.080	0.771	-	0.121	0.760	-	0.154	0.844	-	0.071	0.719	0.751	0.091	0.738	0.719	0.093
MDF [47]	2015	0.831	0.764	0.108	0.759	0.692	0.142	0.785	0.674	0.155	-	-	-	0.694	0.703	0.092	0.730	0.723	0.094
LEGS [59]	2015	0.827	0.787	0.118	0.756	0.682	0.157	0.707	0.661	0.215	0.770	-	0.118	0.669	-	0.133	0.655	-	0.138
BSCA [60]	2015	0.758	0.725	0.183	0.666	0.633	0.224	0.634	0.622	0.266	0.723	0.700	0.174	0.616	0.652	0.191	0.597	0.630	0.197
DRFI [9]	2013	0.786	-	0.164	0.698	-	0.207	0.697	-	0.223	0.777	-	0.145	-	-	-	0.647	-	0.175

two rounds of recurrent translations, each pixel can obtain context features from the global domain adaptively aggregated with different attenuations; see Figure 3(c). In the end, we further perform a 1×1 convolution followed by the group normalization and ReLU non-linear operation on the integrated features to produce the SAC module output, i.e., the spatial attenuation context.

B. Training and Testing Strategies

We built our SAC-Net on ResNet-101 [61] and used the feature pyramid network (FPN) [51] (green blocks in Figure 2) to enhance the feature’s expressiveness. Like [51], we set the channel number of each FPN or SAC layer as 256 and did not use the feature maps at the first layer in both the FPN or SAC module due to the large memory footprint.

Loss function. We used the cross-entropy loss to train the network. Since we have multiple predictions over different layers (from deep to shallow) in our SAC-Net (see Figure 2), the total loss L is defined as the summation of the cross-entropy loss over all the predicted saliency maps:

$$L = - \sum_l \sum_{i,j} g_{i,j} \log(p_{i,j}^l) - (1 - g_{i,j}) \log(1 - p_{i,j}^l), \quad (5)$$

where l is the layer index in network, $g_{i,j}$ is the ground truth value at pixel (i, j) (i.e., one for salient regions, and zero,

otherwise), and $p_{i,j}^l \in [0, 1]$ is the predicted saliency value at pixel (i, j) on the result in the network’s l -th layer.

Training parameters. We initialized the feature extraction part in our network (frontal blue blocks in Figure 2) using weights of ResNet-101 [61] trained on ImageNet [63], and initialized other network parts using random noise. Moreover, we adopted two different training strategies to optimize the network. First, we used stochastic gradient descent (SGD) with a momentum value of 0.9 and a weight decay of 0.0005, and we set the learning rate as 10^{-8} , adjusted it to be 10^{-9} after 13,000 training iterations, and stopped the training after 20,000 iterations. Second, following [29], we used Adam [64] with the first momentum value of 0.9, second momentum value of 0.999, and weight decay of 5×10^4 . We set the learning rate as 10^{-5} and stopped the training after 50,000 iterations. The first training strategy is fast while the second strategy achieves better results; see Section IV-C. Also, we horizontally flipped the input images for data argumentation in both training strategies. Lastly, we trained the network on a single NVidia Titan Xp GPU with a mini-batch size of one and updated the weights in every ten training iterations.

Inference. We took the highest-resolution prediction as the overall result and refined the salient object boundary using fully-connected conditional random field (CRF) [65].

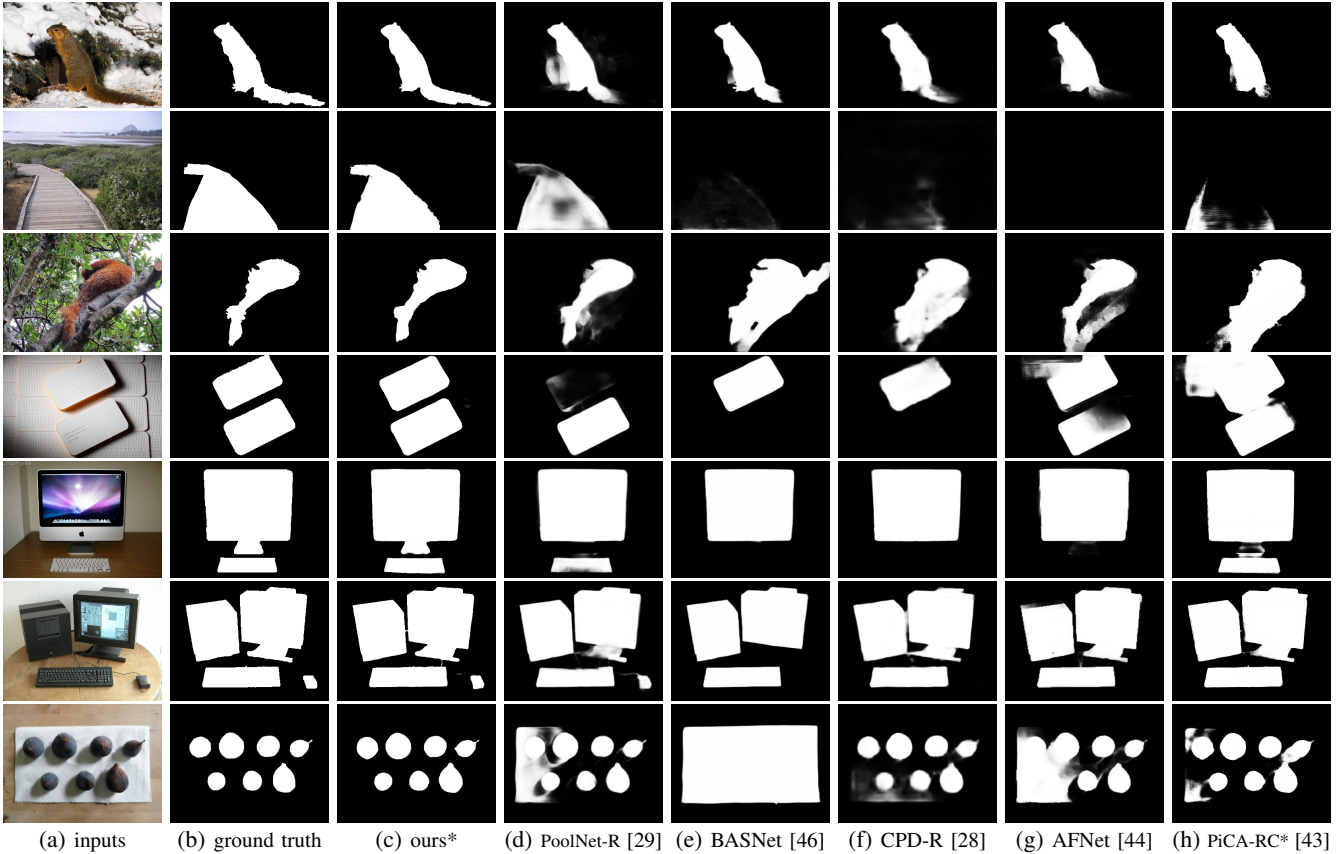


Fig. 5: Visual comparison of saliency maps (c)-(h) produced by different methods. Apparently, our method produces more accurate saliency maps, where “*” indicates CRF is used as a post-processing step in the methods.

IV. EXPERIMENTAL RESULTS

A. Datasets and Evaluation Metrics

We used six widely-used saliency benchmark datasets in our experiments: (i) ECSSD [37] has 1,000 natural images with many semantically meaningful but complex structures; (ii) PASCAL-S [48] has 850 images generated from the PASCAL VOC2010 segmentation dataset [66], where each image has several salient objects; (iii) SOD [54] has 300 images selected from the BSDS dataset [49], where the salient objects are typically of low contrast or closely contact with the image boundary; (iv) HKU-IS [47] has 4,447 images, where most images have multiple salient objects; (v) DUT-OMRON [38] has 5,168 high-quality images, each with one or more salient objects; and (vi) DUTS [50] has a training set of 10,553 images and a testing set (denoted as DUTS-test) of 5,019 images, where the images contain various number of salient objects with large variance in scale. Among the datasets, HKU-IS, DUT-OMRON, and DUTS provide a large number of test images captured under different situations, enabling more comprehensive comparisons among different methods. Moreover, we follow the recent works on salient object detection [43], [41], [22], [24] to train our network model using the training set of DUTS [50].

Next, we used three common metrics for quantitative evaluation: F-measure (F_β), structure measure (S_m) and mean absolute error (MAE), where a large F_β or S_m and a small MAE

indicate a better result; see [67], [18] for their formulations. Also, we used the implementation of [67], [18] to compute F_β , S_m and MAE for all results.

B. Comparison with the State-of-the-arts

We compared our method with 29 state-of-the-art methods; see the first column in Table I. Among the methods, to detect salient objects, BSCA [60] and DRFI [9] use hand-crafted features, while others employ deep neural networks to learn features. For a fair comparison, we obtained their results either by using the saliency maps provided by the authors or by producing the results using their implementations with the released training models.

Quantitative comparison. Table I summarizes the quantitative results compared with the 29 state-of-the-art methods in terms of F_β , S_m and MAE on detecting salient objects in the six benchmark datasets. Our SAC-Net performs favorably against all the others for almost all the cases, regardless of whether CRF is used as a post-processing step. Especially, our method without CRF (SAC-Net) already achieves the best performance compared with all the other methods with CRF for most datasets. This result demonstrates the strong capability of our method to deal with challenging inputs; see also the visual comparison results presented in Figure 5.

Recent deep learning methods use different kinds of backbone networks for feature extraction. For a fair comparison,

TABLE II: Comparing our method (SAC-Net) with the state-of-the-art methods using ResNet-101 as the backbone network. Results are reported before using CRF.

Dataset & Size	-	ECSSD [37] 1,000 images			PASCAL-S [48] 850 images			SOD [54] 300 images			HKU-IS [47] 4,447 images			DUT-OMRON [38] 5,168 images			DUTS-test [50] 5,019 images		
		Year	F_β	S_m	MAE	F_β	S_m	MAE	F_β	S_m	MAE	F_β	S_m	MAE	F_β	S_m	MAE	F_β	S_m
SAC-Net (ours)	-	0.951	0.931	0.031	0.879	0.806	0.070	0.882	0.809	0.093	0.942	0.925	0.026	0.830	0.849	0.052	0.895	0.883	0.034
PoolNet-R+	2019	0.947	0.924	0.032	0.867	0.801	0.071	0.872	0.798	0.097	0.937	0.919	0.026	0.813	0.834	0.052	0.883	0.873	0.035
BASNet+	2019	0.919	0.894	0.049	0.825	0.761	0.101	0.825	0.754	0.126	0.912	0.893	0.040	0.795	0.819	0.064	0.822	0.821	0.061
DSS+ [62]	2019	0.906	0.862	0.074	0.819	0.721	0.115	0.831	0.735	0.144	0.904	0.869	0.054	0.783	0.799	0.070	0.819	0.809	0.067
PiCA-R+	2018	0.940	0.914	0.037	0.863	0.791	0.076	0.864	0.768	0.101	0.931	0.905	0.031	0.816	0.828	0.068	0.868	0.844	0.043

TABLE III: Component analysis. Note that ‘‘SC’’ denotes ‘‘spatial context,’’ ‘‘TS’’ denotes ‘‘training strategy,’’ and ‘‘with LSTM’’ denotes the use of long short-term memory to aggregate the spatial context features.

	SC	TS	ECSSD			PASCAL-S			SOD			HKU-IS			DUT-OMRON			DUTS-test		
			F_β	S_m	MAE	F_β	S_m	MAE	F_β	S_m	MAE	F_β	S_m	MAE	F_β	S_m	MAE	F_β	S_m	MAE
FPN [51]	×	SGD	0.926	0.904	0.056	0.859	0.780	0.085	0.846	0.772	0.124	0.913	0.898	0.046	0.805	0.825	0.065	0.858	0.852	0.052
SAC-Net	√	SGD	0.949	0.928	0.036	0.878	0.805	0.072	0.874	0.806	0.099	0.938	0.923	0.030	0.828	0.849	0.055	0.888	0.879	0.038
	√	Adam	0.951	0.931	0.031	0.879	0.806	0.070	0.882	0.809	0.093	0.942	0.925	0.026	0.830	0.849	0.052	0.895	0.883	0.034
with LSTM	√	SGD	0.941	0.920	0.040	0.872	0.794	0.074	0.860	0.778	0.111	0.930	0.912	0.034	0.825	0.836	0.054	0.881	0.871	0.040

we retrained these methods (PoolNet [29], BASNet [46], and PiCA [43]) by using the same backbone network (ResNet-101) as our SAC-Net. We reported the results of DSS [62] using ResNet-101 by downloading the trained model from the authors’ website. These models are denoted as ‘‘XX+’’. Table II shows the comparison results, where our method still outperforms the very recent salient object detection methods on all the benchmark datasets.

Visual comparison. Figure 5 presents salient object detection results produced by various methods, including ours. From the figures, we can see that other methods (d)-(h) tend to include non-salient backgrounds or miss some salient details, while our SAC-Net is able to produce results (c) that are more consistent with the ground truths (b). Particularly, for challenging cases, such as (i) salient objects and non-salient background with similar appearance (see 1st and 3rd to 5th rows), (ii) small salient objects (see 6th and 7th rows), (iii) complex shapes (see 1st, 3rd, and 5th to 7th rows), and (iv) multiple objects (see 4th to 7th rows), our method can still predict more plausible saliency maps than the others, showing the robustness and quality of SAC-Net.

C. Evaluation on the Network Design

Component analysis. We performed an ablation study to evaluate the major components in SAC-Net. The first row of Table III shows the results from a basic model (FPN [51]) built with only the feature pyramid; see the green blocks in Figure 2. By having the SAC modules in the network to adaptively aggregate spatial context, we can see clear improvements on all the benchmark datasets as compared with the FPN results; see the first two rows in the table.

Training strategy analysis. As mentioned in Section III-B, we adopted two different training strategies to optimize the network. The second and third rows in Table III show the comparison results, where using Adam achieves better results than using SGD. However, ‘‘Adam’’ took around 45 hours to train the model, while ‘‘SGD’’ took only around 15 hours. Hence, we adopted ‘‘SGD’’ to perform the following experiments to evaluate network design.

Compare with LSTM. The long short-term memory [68] (LSTM) is an efficient recurrent neural network to process sequence data by using a set of gates. The method has been extended to process 2D spatial information by some recent works on image classification [69] and saliency detection (s.t., DSCLRCN [42] and PiCA [43]). We performed another experiment by adopting the LSTMs in four principal directions with two rounds of recurrent translations to replace our recurrently-attenuating translation model in the SAC module; in detail, we replaced the feature maps with colored arrows in Figure 4 by the LSTMs in corresponding directions.

The last row in Table III presents the LSTM results. Comparing with our results in the second row, we can see that our method performs better for F_β , S_m and MAE on all the benchmark data. We think the reason is that due to the limitation of the gate functions in LSTM [70], context features can only propagate over a short distance, thus limiting the dispersal of local context features in the spatial domain. On the other hand, the time complexity of computing LSTMs on 2D feature maps is very high. ‘‘with LSTM’’ took around 213 hours to train the model, while our method took only around 15 hours, which is more than 14 times faster.

Architecture analysis. To build our network, we empirically determine the value of n , which affects the number of attenuation factors and the number of feature channels in each aggregated feature map ($\lfloor \frac{256}{n} \rfloor$); see Figure 4. In general, a large n allows the network to consider more variety of attenuation factors but each feature map would capture less information in return, since we keep the overall memory consumption to be manageable. Another parameter in our network is β , where we automatically learn its value for regulating the magnitude of the negative part in Eq. (1).

We evaluated our network on the three largest datasets (HKU-IS, DUT-OMRON, and DUTS-test) using different n and learnable/fixed β . The results shown in Table IV reveal that when we aggregate the image context using two different attenuation factors ($n=2$), we achieve better results than using only one single long-range aggregation ($n=1$). The results

TABLE IV: Architecture analysis of SAC module. “ n ” is the number of attenuation factors and β is defined in Eq. (1); see Sec. III-A. Results are reported before using CRF.

n	β	HKU-IS			DUT-OMRON			DUTS-test		
		F_β	S_m	MAE	F_β	S_m	MAE	F_β	S_m	MAE
1	learnable	0.928	0.914	0.035	0.824	0.836	0.058	0.875	0.866	0.043
2	learnable	0.937	0.921	0.031	0.826	0.843	0.057	0.886	0.877	0.039
3	learnable	0.938	0.923	0.030	0.828	0.849	0.055	0.888	0.879	0.038
4	learnable	0.937	0.922	0.030	0.829	0.846	0.056	0.888	0.878	0.038
5	learnable	0.937	0.921	0.031	0.825	0.844	0.057	0.887	0.878	0.039
3	fixed (0.1)	0.936	0.921	0.031	0.825	0.846	0.056	0.887	0.877	0.039
3	fixed (0)	0.936	0.922	0.030	0.824	0.844	0.058	0.883	0.875	0.040
3	fixed (1)	0.935	0.920	0.032	0.826	0.846	0.057	0.884	0.875	0.041

further improve with larger n and roughly stabilizes when n reaches three, so we set $n=3$. On the other hand, comparing the results on the 3rd and last three rows (all with $n=3$) in table, we can see that automatically learning and adjusting β gives better results than using a fixed β ($\beta = 0.1$ or 0), or linearly aggregating the spatial features ($\beta = 1$).

Attention weight visualization. Figures 1 & 6 visualize the learned attention weights for integrating the spatial context features. The long-range context (c) helps to locate the global background regions; the medium-range context (d) helps to identify the image regions of objects; and short-range context (e) helps to locate the boundary between salient and non-salient regions. Moreover, our attention mechanism selectively aggregates various spatial context and allows the context features to be implicitly dispersed over arbitrary spatial ranges.

Time performance. Our network is fast, since it has a fully convolutional architecture and employs an efficient recurrent translation module. We trained and tested our network on a single GPU (TITAN Xp) using input images of size 400×400 . It takes ~ 0.09 second on average to test one image. To post-process an image with the CRF, it takes another 0.5 second.

D. Discussion

There has been a lot of works on exploiting spatial context in deep CNNs for image analysis. Dilated convolution [71], [72] takes context from larger regions by inserting holes into the convolution kernels, but the context information in use still has a fixed range in a local region. ASPP [73], [74] and PSPNet [75] adopt multiple convolution kernels with different dilated rates or multiple pooling operations with different scales to aggregate spatial context using different region sizes; however, their designed kernel or pooling sizes are fixed, less flexible, and not adaptable to different inputs. DSC [76], [77] adopts the attention weights to indicate the importance of context features aggregated from different directions, but it only obtains the global context with a fixed influence range over the spatial domain. The non-local network [32] computes correlations between every pixel pair on the feature map to encode the global image semantics, but this method ignores the spatial relationship between pixels in the aggregation; for salient object detection, features of opposite semantics may, however, be important; see Figure 1. PSANet [78] adaptively learns attention weights for each pixel to aggregate the information from different positions; however, it is unable

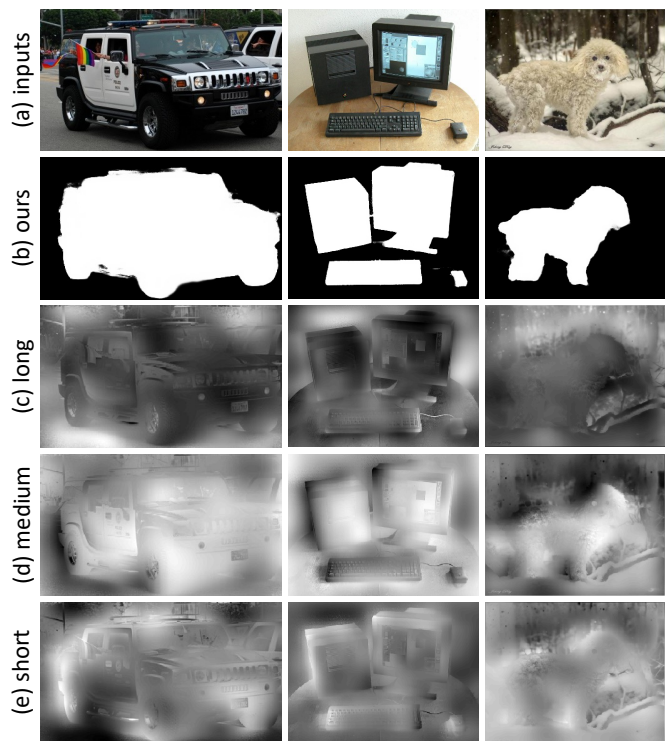


Fig. 6: Attention weights learned for different spatial ranges, where the brightness indicates the magnitude of the learned attention weights.

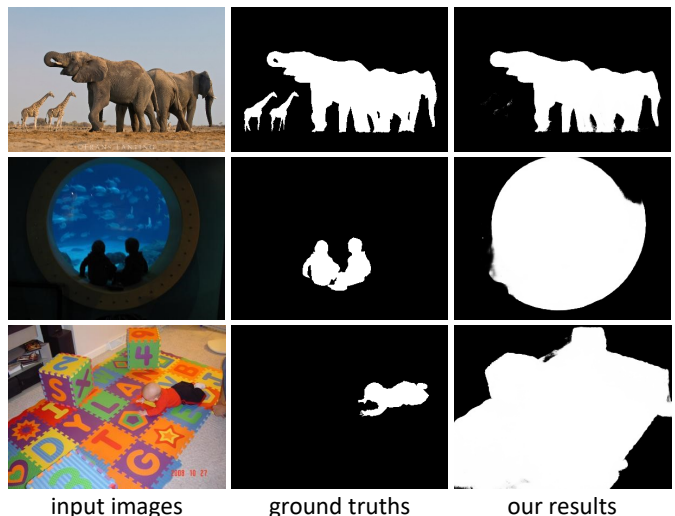


Fig. 7: Three typical failure cases.

to capture the context on lower-level feature maps in high resolutions due to the huge time and memory overhead. Compared to these methods, our SAC-Net explores and adaptively aggregates context features implicitly with variable influence ranges; it is flexible, fast, and computationally friendly for efficient salient object detection.

Lastly, we also analyzed the failure cases, for which we found to be highly challenging, also for the other state-of-the-art methods. For instance, our method may fail for (i) multiple salient objects in very different scales (see Figure 7 (top)),

where the network may regard the small objects as non-salient background; (ii) dark salient objects (see Figure 7 (middle)), where there are insufficient context to determine whether the regions are salient or not; and (iii) salient objects over a complex background (see Figure 7 (bottom)), where high-level scene knowledge is required to understand the image.

We will release our code, the trained models, and the predicted saliency maps on all the benchmark datasets upon the publication of this work.

V. CONCLUSION

This paper presents a novel saliency detection network based on the spatial attenuation context. Our key idea is to recurrently propagate and aggregate image context with different attenuation factors and to integrate the aggregated features using weights learnt from an attention mechanism. Using our model, local image context can adaptively propagate over different ranges, and we can leverage the complementary advantages of these context to improve the saliency detection quality. In the end, we evaluated our method on six common benchmark datasets and compared it extensively with 29 state-of-the-art methods. Experimental results clearly show that our method performs favorably over all the others, both visually and quantitatively. In the future, we plan to explore the potential of our SAC module design for instance-level salient object detection and enhance its capability for detecting salient objects in videos.

REFERENCES

- [1] W. Wang, J. Shen, and F. Porikli, "Saliency-aware geodesic video object segmentation," in *CVPR*, 2015, pp. 3395–3402.
- [2] S. Hong, T. You, S. Kwak, and B. Han, "Online tracking by learning discriminative saliency map with convolutional neural network," in *ICML*, 2015, pp. 597–606.
- [3] H. Hadizadeh and I. V. Bajic, "Saliency-aware video compression," *IEEE Transactions on Image Processing*, vol. 23, no. 1, pp. 19–33, 2014.
- [4] H. Zhao, X. Mao, X. Jin, J. Shen, F. Wei, and J. Feng, "Real-time saliency-aware video abstraction," *The Visual Computer*, vol. 25, no. 11, pp. 973–984, 2009.
- [5] M.-M. Cheng, F.-L. Zhang, N. J. Mitra, X. Huang, and S.-M. Hu, "Repfinder: Finding approximately repeated scene elements for image editing," in *ACM Trans. on Graphics (SIGGRAPH)*, vol. 29, no. 4, ACM, 2010, p. 83.
- [6] L. Zhu, X. Hu, C.-W. Fu, J. Qin, and P.-A. Heng, "Saliency-aware texture smoothing," *IEEE Transactions on Visualization and Computer Graphics*, 2018.
- [7] H. Zhang, J. Zhang, and P. Koniusz, "Few-shot learning via saliency-guided hallucination of samples," in *CVPR*, 2019, pp. 2770–2779.
- [8] M.-M. Cheng, N. J. Mitra, X. Huang, P. H. Torr, and S.-M. Hu, "Global contrast based salient region detection," *IEEE Transactions on Pattern Analysis and Machine Intelligence*, vol. 37, no. 3, pp. 569–582, 2015.
- [9] H. Jiang, J. Wang, Z. Yuan, Y. Wu, N. Zheng, and S. Li, "Salient object detection: A discriminative regional feature integration approach," in *CVPR*, 2013, pp. 2083–2090.
- [10] T. Liu, Z. Yuan, J. Sun, J. Wang, N. Zheng, X. Tang, and H.-Y. Shum, "Learning to detect a salient object," *IEEE Transactions on Pattern Analysis and Machine Intelligence*, vol. 33, no. 2, pp. 353–367, 2011.
- [11] X. Li, L. Zhao, L. Wei, M.-H. Yang, F. Wu, Y. Zhuang, H. Ling, and J. Wang, "DeepSaliency: Multi-task deep neural network model for salient object detection," *IEEE Transactions on Image Processing*, vol. 25, no. 8, pp. 3919–3930, 2016.
- [12] Z. Luo, A. Mishra, A. Achkar, J. Eichel, S. Li, and P.-M. Jodoin, "Non-local deep features for salient object detection," in *CVPR*, 2017, pp. 6609–6617.
- [13] L. Wang, L. Wang, H. Lu, P. Zhang, and X. Ruan, "Saliency detection with recurrent fully convolutional networks," in *ECCV*, 2016, pp. 825–841.
- [14] P. Zhang, D. Wang, H. Lu, H. Wang, and B. Yin, "Learning uncertain convolutional features for accurate saliency detection," in *ICCV*, 2017, pp. 212–221.
- [15] R. Zhao, W. Ouyang, H. Li, and X. Wang, "Saliency detection by multi-context deep learning," in *CVPR*, 2015, pp. 1265–1274.
- [16] S. Chen, X. Tan, B. Wang, and X. Hu, "Reverse attention for salient object detection," in *ECCV*, 2018.
- [17] Z. Deng, X. Hu, L. Zhu, X. Xu, J. Qin, G. Han, and P.-A. Heng, "R³Net: Recurrent residual refinement network for saliency detection," in *IJCAI*, 2018, pp. 684–690.
- [18] Q. Hou, M.-M. Cheng, X. Hu, A. Borji, Z. Tu, and P. H. Torr, "Deeply supervised salient object detection with short connections," in *CVPR*, 2017, pp. 3203–3212.
- [19] X. Hu, L. Zhu, J. Qin, C.-W. Fu, and P.-A. Heng, "Recurrently aggregating deep features for salient object detection," in *AAAI*, 2018, pp. 6943–6950.
- [20] G. Li and Y. Yu, "Deep contrast learning for salient object detection," in *CVPR*, 2016, pp. 478–487.
- [21] X. Li, F. Yang, H. Cheng, W. Liu, and D. Shen, "Contour knowledge transfer for salient object detection," in *ECCV*, 2018.
- [22] L. Zhang, J. Dai, H. Lu, Y. He, and G. Wang, "A bi-directional message passing model for salient object detection," in *CVPR*, 2018, pp. 1741–1750.
- [23] P. Zhang, D. Wang, H. Lu, H. Wang, and X. Ruan, "Amulet: Aggregating multi-level convolutional features for salient object detection," in *ICCV*, 2017, pp. 202–211.
- [24] X. Zhang, T. Wang, J. Qi, H. Lu, and G. Wang, "Progressive attention guided recurrent network for salient object detection," in *CVPR*, 2018, pp. 714–722.
- [25] P. Zhang, W. Liu, H. Lu, and C. Shen, "Salient object detection with lossless feature reflection and weighted structural loss," *IEEE Transactions on Image Processing*, vol. 28, no. 6, pp. 3048–3060, 2019.
- [26] W. Wang, S. Zhao, J. Shen, S. C. Hoi, and A. Borji, "Salient object detection with pyramid attention and salient edges," in *CVPR*, 2019, pp. 1448–1457.
- [27] T. Zhao and X. Wu, "Pyramid feature attention network for saliency detection," in *CVPR*, 2019, pp. 3085–3094.
- [28] Z. Wu, L. Su, and Q. Huang, "Cascaded partial decoder for fast and accurate salient object detection," in *CVPR*, 2019, pp. 3907–3916.
- [29] J.-J. Liu, Q. Hou, M.-M. Cheng, J. Feng, and J. Jiang, "A simple pooling-based design for real-time salient object detection," in *CVPR*, 2019, pp. 3917–3926.
- [30] W. Wang, J. Shen, M.-M. Cheng, and L. Shao, "An iterative and cooperative top-down and bottom-up inference network for salient object detection," in *CVPR*, 2019, pp. 5968–5977.
- [31] R. Wu, M. Feng, W. Guan, D. Wang, H. Lu, and E. Ding, "A mutual learning method for salient object detection with intertwined multi-supervision," in *CVPR*, 2019, pp. 8150–8159.
- [32] X. Wang, R. Girshick, A. Gupta, and K. He, "Non-local neural networks," in *CVPR*, 2018, pp. 7794–7803.
- [33] S. Goferman, L. Zelnik-Manor, and A. Tal, "Context-aware saliency detection," *IEEE Transactions on Pattern Analysis and Machine Intelligence*, vol. 34, no. 10, pp. 1915–1926, 2012.
- [34] F. Perazzi, P. Krähenbühl, Y. Pritch, and A. Hornung, "Saliency filters: Contrast based filtering for salient region detection," in *CVPR*, 2012, pp. 733–740.
- [35] A. Borji and L. Itti, "Exploiting local and global patch rarities for saliency detection," in *CVPR*, 2012, pp. 478–485.
- [36] V. Mahadevan and N. Vasconcelos, "Biologically inspired object tracking using center-surround saliency mechanisms," *IEEE Transactions on Pattern Analysis and Machine Intelligence*, vol. 35, no. 3, pp. 541–554, 2013.
- [37] Q. Yan, L. Xu, J. Shi, and J. Jia, "Hierarchical saliency detection," in *CVPR*, 2013, pp. 1155–1162.
- [38] C. Yang, L. Zhang, H. Lu, X. Ruan, and M.-H. Yang, "Saliency detection via graph-based manifold ranking," in *CVPR*, 2013, pp. 3166–3173.
- [39] J. Harel, C. Koch, and P. Perona, "Graph-based visual saliency," in *NIPS*, 2007, pp. 545–552.
- [40] A. Borji, M.-M. Cheng, H. Jiang, and J. Li, "Salient object detection: A benchmark," *IEEE Transactions on Image Processing*, vol. 24, no. 12, pp. 5706–5722, 2015.
- [41] T. Wang, L. Zhang, S. Wang, H. Lu, G. Yang, X. Ruan, and A. Borji, "Detect globally, refine locally: A novel approach to saliency detection," in *CVPR*, 2018, pp. 3127–3135.
- [42] N. Liu and J. Han, "A deep spatial contextual long-term recurrent convolutional network for saliency detection," *IEEE Transactions on Image Processing*, vol. 27, no. 7, pp. 3264–3274, 2018.

- [43] N. Liu, J. Han, and M.-H. Yang, "PiCANet: Learning pixel-wise contextual attention for saliency detection," in *CVPR*, 2018, pp. 3089–3098.
- [44] M. Feng, H. Lu, and E. Ding, "Attentive feedback network for boundary-aware salient object detection," in *CVPR*, 2019, pp. 1623–1632.
- [45] L. Zhang, J. Zhang, Z. Lin, H. Lu, and Y. He, "CapSal: Leveraging captioning to boost semantics for salient object detection," in *CVPR*, 2019, pp. 6024–6033.
- [46] X. Qin, Z. Zhang, C. Huang, C. Gao, M. Dehghan, and M. Jagersand, "BASNet: Boundary-aware salient object detection," in *CVPR*, 2019, pp. 7479–7489.
- [47] G. Li and Y. Yu, "Visual saliency based on multiscale deep features," in *CVPR*, 2015, pp. 5455–5463.
- [48] Y. Li, X. Hou, C. Koch, J. M. Rehg, and A. L. Yuille, "The secrets of salient object segmentation," in *CVPR*, 2014, pp. 280–287.
- [49] D. Martin, C. Fowlkes, D. Tal, and J. Malik, "A database of human segmented natural images and its application to evaluating segmentation algorithms and measuring ecological statistics," in *ICCV*, 2001, pp. 416–423.
- [50] L. Wang, H. Lu, Y. Wang, M. Feng, D. Wang, B. Yin, and X. Ruan, "Learning to detect salient objects with image-level supervision," in *CVPR*, 2017, pp. 136–145.
- [51] T.-Y. Lin, P. Dollár, R. Girshick, K. He, B. Hariharan, and S. Belongie, "Feature pyramid networks for object detection," in *CVPR*, 2017, pp. 2117–2125.
- [52] Y. Wu and K. He, "Group normalization," in *ECCV*, 2018, pp. 3–19.
- [53] A. Krizhevsky, I. Sutskever, and G. E. Hinton, "ImageNet classification with deep convolutional neural networks," in *NIPS*, 2012, pp. 1097–1105.
- [54] V. Movahedi and J. H. Elder, "Design and perceptual validation of performance measures for salient object segmentation," in *CVPRW*, 2010, pp. 49–56.
- [55] W. Wang, J. Shen, X. Dong, and A. Borji, "Salient object detection driven by fixation prediction," in *CVPR*, 2018, pp. 1711–1720.
- [56] T. Wang, A. Borji, L. Zhang, P. Zhang, and H. Lu, "A stagewise refinement model for detecting salient objects in images," in *CVPR*, 2017, pp. 4019–4028.
- [57] N. Liu and J. Han, "DHSNet: Deep hierarchical saliency network for salient object detection," in *CVPR*, 2016, pp. 678–686.
- [58] G. Lee, Y.-W. Tai, and J. Kim, "Deep saliency with encoded low level distance map and high level features," in *CVPR*, 2016, pp. 660–668.
- [59] L. Wang, H. Lu, X. Ruan, and M.-H. Yang, "Deep networks for saliency detection via local estimation and global search," in *CVPR*, 2015, pp. 3183–3192.
- [60] Y. Qin, H. Lu, Y. Xu, and H. Wang, "Saliency detection via cellular automata," in *CVPR*, 2015, pp. 110–119.
- [61] K. He, X. Zhang, S. Ren, and J. Sun, "Deep residual learning for image recognition," in *CVPR*, 2016, pp. 770–778.
- [62] Q. Hou, M. Cheng, X. Hu, A. Borji, Z. Tu, and P. Torr, "Deeply supervised salient object detection with short connections," *IEEE Transactions on Pattern Analysis and Machine Intelligence*, vol. 41, no. 4, p. 815, 2019.
- [63] J. Deng, W. Dong, R. Socher, L.-J. Li, K. Li, and L. Fei-Fei, "ImageNet: A large-scale hierarchical image database," in *CVPR*, 2009, pp. 248–255.
- [64] D. P. Kingma and J. Ba, "Adam: A method for stochastic optimization," in *ICLR*, 2015.
- [65] P. Krähenbühl and V. Koltun, "Efficient inference in fully connected CRFs with Gaussian edge potentials," in *NIPS*, 2011, pp. 109–117.
- [66] M. Everingham, L. Van Gool, C. K. Williams, J. Winn, and A. Zisserman, "The pascal visual object classes (VOC) challenge," *International Journal of Computer Vision*, vol. 88, no. 2, pp. 303–338, 2010.
- [67] D.-P. Fan, M.-M. Cheng, Y. Liu, T. Li, and A. Borji, "Structure-measure: A new way to evaluate foreground maps," in *ICCV*, 2017, pp. 4548–4557.
- [68] S. Hochreiter and J. Schmidhuber, "Long short-term memory," *Neural computation*, vol. 9, no. 8, pp. 1735–1780, 1997.
- [69] F. Visin, K. Kastner, K. Cho, M. Matteucci, A. Courville, and Y. Bengio, "ReNet: A recurrent neural network based alternative to convolutional networks," *arXiv preprint arXiv:1505.00393*, 2015.
- [70] Q. V. Le, N. Jaitly, and G. E. Hinton, "A simple way to initialize recurrent networks of rectified linear units," *arXiv preprint arXiv:1504.00941*, 2015.
- [71] L.-C. Chen, G. Papandreou, I. Kokkinos, K. Murphy, and A. L. Yuille, "Semantic image segmentation with deep convolutional nets and fully connected CRFs," in *ICLR*, 2015.
- [72] F. Yu and V. Koltun, "Multi-scale context aggregation by dilated convolutions," in *ICLR*, 2016.
- [73] L.-C. Chen, G. Papandreou, I. Kokkinos, K. Murphy, and A. L. Yuille, "Deeplab: Semantic image segmentation with deep convolutional nets, atrous convolution, and fully connected CRFs," *IEEE Transactions on Pattern Analysis and Machine Intelligence*, vol. 40, no. 4, pp. 834–848, 2018.
- [74] L.-C. Chen, G. Papandreou, F. Schroff, and H. Adam, "Rethinking atrous convolution for semantic image segmentation," *arXiv preprint arXiv:1706.05587*, 2017.
- [75] H. Zhao, J. Shi, X. Qi, X. Wang, and J. Jia, "Pyramid scene parsing network," in *CVPR*, 2017, pp. 2881–2890.
- [76] X. Hu, L. Zhu, C.-W. Fu, J. Qin, and P.-A. Heng, "Direction-aware spatial context features for shadow detection," in *CVPR*, 2018, pp. 7454–7462.
- [77] X. Hu, C.-W. Fu, L. Zhu, J. Qin, and P.-A. Heng, "Direction-aware spatial context features for shadow detection and removal," *IEEE Transactions on Pattern Analysis and Machine Intelligence*, 2019.
- [78] H. Zhao, Y. Zhang, S. Liu, J. Shi, C. Change Loy, D. Lin, and J. Jia, "PSANet: Point-wise spatial attention network for scene parsing," in *ECCV*, 2018, pp. 267–283.